White Rose Research Online

eprints@whiterose.ac.uk
https://eprints.whiterose.ac.uk
Universities of Leeds, Sheffield and York

Deposited via The University of Sheffield.

White Rose Research Online URL for this paper:
https://eprints.whiterose.ac.uk/id/eprint/126513/

Version: Published Version

Article:
Nguyen, N.B., Nielsen, M.P., Lafone, L. et al. (2017) Hybrid gap plasmon GaAs nanolasers. Applied Physics Letters, 111 (26). 261107. ISSN: 0003-6951

https://doi.org/10.1063/1.5008320

Reuse
Items deposited in White Rose Research Online are protected by copyright, with all rights reserved unless indicated otherwise. They may be downloaded and/or printed for private study, or other acts as permitted by national copyright laws. The publisher or other rights holders may allow further reproduction and re-use of the full text version. This is indicated by the licence information on the White Rose Research Online record for the item.

Takedown
If you consider content in White Rose Research Online to be in breach of UK law, please notify us by emailing eprints@whiterose.ac.uk including the URL of the record and the reason for the withdrawal request.

UNIVERSITY OF LEEDS
University of Sheffield
UNIVERSITY of York

Hybrid gap plasmon GaAs nanolasers

Ngoc B. Nguyen, Michael P. Nielsen, Lucas Lafone, Edmund Clarke, Paul Fry, and Rupert F. Oulton

Citation: Appl. Phys. Lett. **111**, 261107 (2017);
View online: https://doi.org/10.1063/1.5008320
View Table of Contents: http://aip.scitation.org/toc/apl/111/26
Published by the American Institute of Physics

Articles you may be interested in

Bidirectional reconfiguration and thermal tuning of microcantilever metamaterial device operating from 77 K to 400 K
Applied Physics Letters **111**, 261101 (2017); 10.1063/1.5006836

Plasma modification of spoof plasmon propagation along metamaterial-air interfaces
Applied Physics Letters **111**, 261105 (2017); 10.1063/1.5006666

Tamm plasmon sub-wavelength structuration for loss reduction and resonance tuning
Applied Physics Letters **111**, 261103 (2017); 10.1063/1.4991025

High transmittance contrast in amorphous to hexagonal phase of $Ge_2Sb_2Te_5$: Reversible NIR-window
Applied Physics Letters **111**, 261102 (2017); 10.1063/1.5009610

Broadband manipulation of refracted wavefronts by gradient acoustic metasurface with V-shape structure
Applied Physics Letters **111**, 263501 (2017); 10.1063/1.5005950

Experimental examination of tunneling paths in SiGe/Si gate-normal tunneling field-effect transistors
Applied Physics Letters **111**, 263504 (2017); 10.1063/1.4996109

Scilight
Sharp, quick summaries illuminating the latest physics research
Sign up for FREE!

APPLIED PHYSICS LETTERS **111**, 261107 (2017)

Hybrid gap plasmon GaAs nanolasers

Ngoc B. Nguyen,[1] Michael P. Nielsen,[1] Lucas Lafone,[1] Edmund Clarke,[2] Paul Fry,[2] and Rupert F. Oulton[1,a)]
[1]*Department of Physics, Imperial College London, London SW7 2AZ, United Kingdom*
[2]*EPSRC National Epitaxy Facility, University of Sheffield, Sheffield S1 4DE, United Kingdom*

(Received 5 October 2017; accepted 11 December 2017; published online 29 December 2017)

Compact semiconductor lasers with sub-wavelength-scale dimensions rely heavily on materials with low surface recombination due to the large surface area to volume ratios of their nano-cavities. Furthermore, the reliance on semiconductor nanostructures has led to predominantly bottom-up fabrication approaches, which has hindered scalable and practical applications. In this letter, we present lithographically constructed hybrid gap plasmon nanolasers using the gain of bulk GaAs operating at room temperature. The nanolasers are built on GaAs suspended membranes with InGaP passivation layers. Laser resonators are defined only by patterning gold on top of these GaAs membranes, thus eliminating the need to etch the semiconductor for optical confinement, which would introduce additional surface recombination. An analysis of the modal gain and losses in these devices suggests that threshold carrier densities in the range of $4\text{–}5 \times 10^{18}$ cm^{-3} are necessary—potentially achievable with current densities as low as 6–8 kA cm^{-2}. *Published by AIP Publishing.*
https://doi.org/10.1063/1.5008320

Effective deployment of semiconductor nanolasers could have many important ramifications, particularly in the development of on-chip optoelectronics and sensors. The theoretical proposal[1] of the spaser by Bergman and Stockman in 2003 triggered a new trend in the nanolaser research community in which the surface plasmon modes of metals are the key to miniaturization. However, due to the relative youth of the field, existing work has focussed primarily on the demonstration of sub-wavelength devices with little consideration of practicality. Since the first demonstration of plasmonic lasers,[2–4] numerous designs have been theoretically proposed and experimentally demonstrated.[5–8] The majority of these designs have followed a bottom-up fabrication strategy and suffer from poor control over device geometry with a random position and dimension. In this paper, we demonstrate the top-down construction of plasmonic lasers on suspended GaAs slab waveguides (WGs), which closely resemble the standard SOI (silicon-on-insulator) platforms of integrated photonics. The proposed design achieves confinement and feedback solely through 2D lithographic patterning of metal on the GaAs membranes and thus eliminates the requirement to etch the semiconductor in order to define the cavity, which avoids the problem of surface recombination.

Hybrid gap plasmon waveguides (HGPWs) offer a way to manage the high ohmic loss in semiconductor-based plasmonic waveguide designs while still retaining excellent sub-wavelength modal confinement via the inclusion of a low index dielectric spacer layer.[9] Figure 1(a) shows a schematic of our hybrid gap plasmon nanolasers and an SEM image of a typical device. Together with a suspended GaAs membrane construction, this structure resembles the stacking of a standard SOI construction and thus obtains modal properties similar to the previously demonstrated HGPWs on SOI.[9–12] The geometric dimensions H, G, and W—the core thickness, spacer thickness, and gap width, respectively—determine the modal characteristics and regimes in which the waveguide operates. The metal layers of region 1 in Fig. 1(a) modify the effective indices of both the TM and TE bound waves. A higher effective index of the TE wave in region 2 produces a bound TE-like waveguide mode with a reasonable lateral confinement: $\Delta n_{\text{lateral}} = n_{\text{TE2}} - n_{\text{TE1}} = 0.13$ for $H = 100$ nm. The spacer thickness controls the effective index contrast of regions 1 and 2 and thus the degree of lateral confinement;

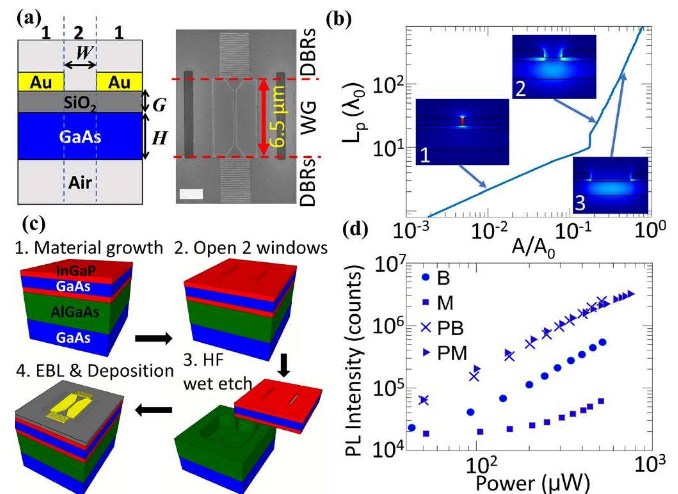

FIG. 1. (a) Cross-sectional schematic of the GaAs HGPW and SEM image of a typical device. Scale bar = 2 μm. $W \sim 195$ nm. (b) Propagation length vs modal area for $W = 5\text{–}3000$ nm. Insets 1, 2, and 3 show the field distribution of the HGPW mode of W = 10 nm, 195 nm, and 800 nm, respectively. Arrows show the corresponding L_p and A/A_0 for each gap width value. Mode Solver Unit under the RF model in COMSOL 4.3a was used to investigate the modal properties of the HGPW. (c) Summary of fabrication steps. (d) PL intensity from samples with and without passivation layers as a function of pump power at $\lambda = 650$ nm, demonstrating the effect of the surface passivation. B, M, PB, and PM stand for the Bulk, Membrane, Passivated Bulk, and Passivated Membrane, respectively.

a)Author to whom correspondence should be addressed: r.oulton@imperial.ac.uk

however, too thin a spacer can lead to a loss of lateral confinement through coupling to TM waves in region 1, $G > G_{\text{critical}} \sim 16\,\text{nm}$. Here, we chose $G = 20\,\text{nm}$ to ensure that the fundamental TE gap mode remains bound. Also shown in Fig. 1(a) is a top-down view SEM image of the fabricated device. The taper sections as part of the waveguide (WG) aim to mitigate modal mismatch arising from an abrupt termination of the waveguide while maintaining adiabatic guiding.[11,13] Feedback is provided by two sets of metallic DBRs (distributed Bragg reflectors) placed at both ends of the WG [see Fig. 1(a)].

Figure 1(b) shows the vacuum wavelength normalized propagation length, $L_p(\lambda_0)$, versus the normalized mode area, A/A_0, for a gap width range of $W = 5$–$3000\,\text{nm}$. Here, we define $A = \frac{\int U(r)dS}{\text{Max}\{2U_E(r)\}}$, with $U = U_E + U_M$ being the total electromagnetic energy and $A_0 = \lambda_0^2/4$.[14] With reference to the field distributions in the insets of Fig. 1(b), it is clear that the increase in the propagation length at larger gap widths can be attributed to a larger contribution of the photonic-like component of the hybrid mode. For a good overlap with the gain media, we chose $W \sim 195\,\text{nm}$, giving a mode overlap with the GaAs core region of ∼80%, a modal area of ∼0.048 λ_0^2, and a modal loss of $\sim 620\,\text{cm}^{-1}$ at $\lambda_0 = 850$ nm.

Figure 1(c) summarizes the fabrication process of the GaAs HGPWs. Etch windows were created using reactive ion etching, followed by HF etching of a sacrificial $2\,\mu\text{m}$ thick $Al_{0.65}Ga_{0.35}As$ layer to create 100 nm thick suspended GaAs membranes. The size of the undercut regions was kept to about $25 \times 20\,\mu\text{m}$ to ensure membrane integrity. The problem of surface recombination in the exposed thin suspended GaAs membrane was overcome by growing two 5 nm thick InGaP layers on either side of the GaAs membrane during MBE (Molecular Beam Epitaxy).[15,16] In Fig. 1(d), photoluminescence (PL) intensities as a function of pump power were plotted for the bulk and membrane regions of passivated and unpassivated samples. PL yields were observed to improve by more than 2 orders of magnitude for the passivated GaAs membranes. In particular, the emission from passivated bulk and passivated membrane regions attained similar PL compared to an order of magnitude difference when both were left unpassivated. Gold was selected as the plasmonic material, instead of lower loss silver, to avoid problems associated with surface roughness and oxidation.[17] The use of metallic gold DBRs to define the cavity enables both the waveguide and the feedback sections to be fabricated in a single lithography step.

The devices were optically pumped near an absorption peak of the geometry at 725 nm with 150 fs laser pulses at a repetition rate of 100 kHz. The signal was collected using a low noise liquid nitrogen cooled Spec-10 Si detector and a Princeton Instruments SP-2300i spectrometer. We pumped the laser using an elongated beam centered along the long axis of the device. The pump wavelength was chosen to maximize absorption in the GaAs core based on the transfer matrix approach. By modelling the pump spot as a 2D Gaussian beam and taking into account the geometry of the pumped region, the absorption in the GaAs gain region was estimated to be 10%, with most of the energy absorbed in the taper regions (∼70%).

The characteristics of a typical lasing device with a grating period of $\Lambda = 150\,\text{nm}$ and $W \approx 195\,\text{nm}$ are summarized in Fig. 2. The 2D CCD detector allows a 1D spatial map of the spectral response of the device to be created. The data were taken from a single horizontal pixel line across the middle of the device. Figure 2(a) shows a clear spectral change in the response of the device when the pump energy is increased. A peak appears in the broad spectral response of the spontaneous emission as stimulated emission begins to dominate. The scattered light is shown to polarize mostly in the direction perpendicular to the long axis of the waveguide, well above 70% TE polarized [see Fig. 2(b)]. This is a clear indication that the lasing response originates from a TE-like hybrid gap mode.

Figure 2(c) presents the integrated intensity of the photoluminescence spectra, I_{int}, as a function of pump energy density, normalized by the simulated pump absorptivity of the device. The kink signature of the onset of lasing is observed here, with amplified spontaneous emission followed by stimulated emission. The lasing characteristic is further emphasized by a reduction in the FWHM (full width at half maximum) followed by a broadening of the lasing peak as the pump continues to increase[18] [see Fig. 2(d)]. By design, the DBRs only give a high reflectivity to the TE HGPW mode travelling in the plane of the membranes while acting as poor out-couplers to the far-field. This means that by collecting emission from the top of the device with a limited collection angle, we effectively only access a small fraction of the laser emission. The extent and behavior of the spontaneous emission background in our data are also influenced by the emission material extending well beyond the lithographically defined cavity. While a laser response will only be achieved in the cavity region, spontaneous emission can emanate from other areas exposed to the pump beam as well as areas pumped by emission from the cavity region. We thus observe regions where the carrier concentration does not clamp at the laser cavity threshold, which has also been observed in other nanoscale laser designs.[19,20]

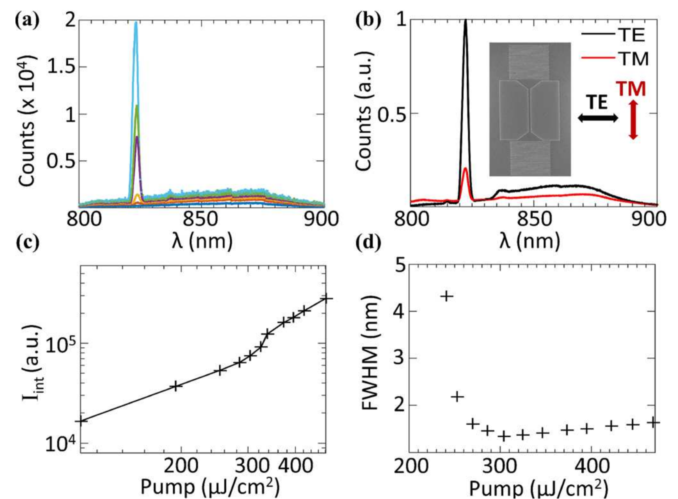

FIG. 2. (a) Spectral response of photoluminescence of the device with increasing pump power. (b) Polarization characteristics of the lasing signal. The data plotted here were taken from the whole device above threshold. (c) Integrated intensity of the signal as a function of pump energy density. (d) FWHM of the lasing signal as a function of pump intensity.

The total cavity losses in these lasers consist of the modal loss $\alpha_{mod}(\lambda)$, which is a function of the HGPW mode's field distribution, and the mirrors loss $\alpha_{mir}(\lambda)$, which defines the feedback efficiency.[21] However, the mirror loss in these devices is fairly high due to limited DBR reflectivity. While the HGPW mode is constrained by $G_{critical}$, the DBRs could be brought closer to the GaAs core to increase DBR reflectivity. We thus considered a second design where the gratings and the waveguide were fabricated in two separate lithography steps (referred to as 2-step devices). Here, the DBRs were placed 10 nm above the GaAs core, while the waveguide and G remain at 20 nm. Owing to the higher DBR reflectivity, 2-step devices had lower lasing thresholds: in this case, a 25% increase in DBR reflectivity resulted in a decrease in lasing threshold by nearly half. This suggests that cavity feedback was the dominant loss mechanism for the single step devices. Following the first lithography step, the corresponding DBR-only devices were also studied to assess the mirror loss, $\alpha_{mir}(\lambda)$. The 2-step devices thus have total loss: $\alpha_{tot}(\lambda) = \alpha_{mod}(\lambda) + \alpha_{mir}(\lambda)$. A DBR-only device consists of two sets of metallic gratings, spaced 10 nm away from the GaAs core, without the waveguide section in-between.

Our analysis of the material gain and carrier concentration of lasing conditions was built upon a simple semiconductor gain model of bulk GaAs and free carrier theory,[22] facilitating the study of nanoscale laser systems in the high pumping regime. Figure 3(a) plots the material gain and its associated induced refractive index, n_{ind}, as a function of wavelength. The band-filling effect leads to a blue-shift in the gain spectra of GaAs as the carrier density gets larger.[21] Our calculated magnitude of free carrier induced refractive index change of GaAs agrees well with experimental values found in the literature.[23,24] An increase in the carrier concentration, N, results in a substantial reduction of the refractive index of GaAs across the wavelength range of interest. Figure 3(b) shows the experimentally observed shift of the lasing peak wavelength as the pump intensity increases for a 2-step device of $W \sim 195$ nm and $\Lambda = 150$ nm. Here, the maximum wavelength value monotonically reduces following the onset of lasing. Meanwhile, a group index, $n_g \approx 6.9$, was determined near threshold via $\Delta\lambda = \lambda^2/2n_gL$, using the three visible laser modes. This exceeds, $n_g = 4.4$, obtained from numerical simulations, the discrepancy arising from the increased dispersion in the high gain regime. This emphasizes the role of carrier induced refractive index changes in the operation of these devices.

Using values of n_{ind} calculated from our gain model, we numerically simulated the in-plane reflection of the DBRs with Lumerical FDTD Solutions for $N \sim 10^{19}$ cm^{-3}. The simulated reflection of the gratings and the experimental data of their corresponding HGPW devices are shown in Figs. 3(c)–3(f) for the case of 2-step devices. Without accounting for the carrier induced refractive index change, simulated DBR reflection bands would be red-shifted by roughly 20 nm with respect to those shown in Fig. 3(c). It is worth noting that the gain bandwidth is roughly twice that of the DBR stop band. The lasing wavelength therefore should fall into the region where the overlap of these two distinct spectral responses gives sufficient gain to overcome the total loss of the device. Figures 3(d)–3(f) suggest DBR reflectivities of ~65%–70% at peak reflection for the three periods considered. By maintaining similar metal gap widths ($W \sim 195$ nm) to ensure similar modal loss, we can assume that regardless of grating periodicity, all 2-step devices have comparable total device loss.

Figure 4(a) shows emission spectra from corresponding DBR-only and 2-step devices near their respective threshold pump conditions. A clear blue shift of the emerging laser peaks [arrows in Fig. 4(a)] occurs for DBR-only and 2-step devices of the same grating period due to the addition of modal losses. These distinct lasing wavelengths reflect the different threshold gain and corresponding carrier concentrations that each device follows. The dependence of gain on the carrier concentration for the four laser wavelengths identified in Fig. 4(a) is plotted in Fig. 4(b). To estimate the threshold gain, we need to know the relationship between

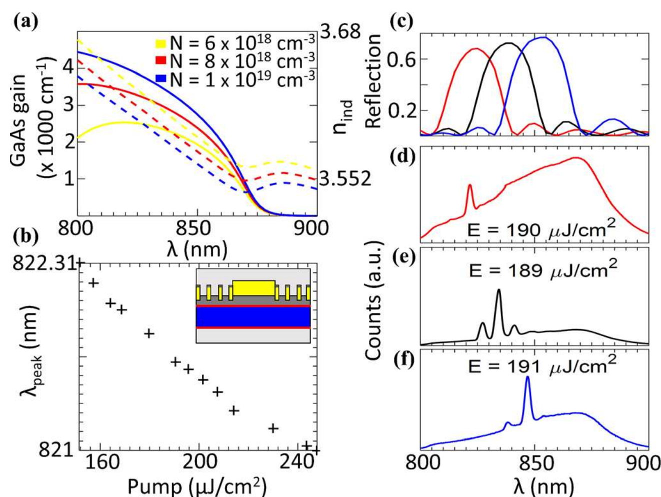

FIG. 3. (a) GaAs material gain and carrier induced refractive index change as a function of wavelength for different values of carrier concentrations, N. Line colors indicate different values of carrier concentrations. (b) Peak wavelength of the observed lasing signals as a function of pump intensity for a typical 2-step device of $W = 195$ nm and $\Lambda = 150$ nm. The inset shows a side view sketch of a typical 2-step device. (c) Numerical simulation of the in-plane reflection of the gratings for three different periods: $\Lambda = 150$ nm, 155 nm, and 160 nm of 2-step devices. (d)–(f) Correspondingly shown here are the spectral responses of these devices at a pump density of $\sim 190\,\mu$J/cm^2, which is just above laser threshold in each case. Line colors show different values of the grating period.

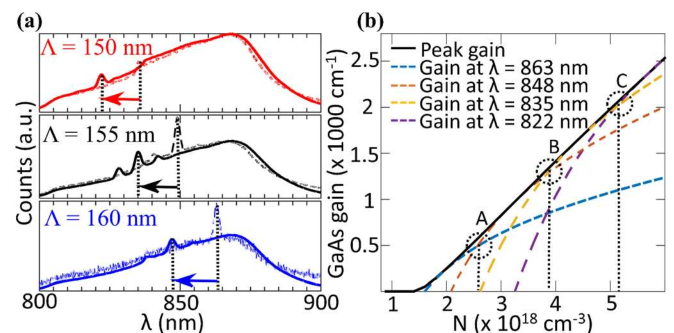

FIG. 4. (a) Photoluminescence spectra of DBR-only devices (dashed lines) and corresponding 2-step devices (solid lines) of the grating periods, $\Lambda = 150$ nm, 155 nm, and 160 nm at power values near threshold (for the 2-step lasers, $W \sim 195$ nm). (b) Peak gain and gain at particular wavelengths plotted as a function of carrier concentration.

threshold pump intensity, $P_{th}(\lambda)$, at a given wavelength and carrier concentration, N_{th}. However, calculating N_{th} directly from $P_{th}(\lambda)$ would involve speculation of various hidden efficiency factors such as pumping conditions, design geometry, and intrinsic gain properties. Nonetheless, by assuming that N_{th} is a monotonic function of $P_{th}(\lambda)$, we can determine bounds for the required threshold gain in our devices.

In the case of the DBR-only devices, the device with $\Lambda = 160\,\text{nm}$ had the lowest lasing threshold, $P_{th}(863\,\text{nm}) < P_{th}(835\,\text{nm}), P_{th}(848\,\text{nm})$, where the lasing wavelengths of DBR-only devices of $\Lambda = 150\,\text{nm}$, 155 nm, and 160 nm are $\lambda \approx 835\,\text{nm}$, 848 nm, and 863 nm, respectively. Hence, point A in Fig. 4(b), which corresponds to $N \approx 2.55 \times 10^{18}\,\text{cm}^{-3}$, sets an upper bound for the mirror loss, $\alpha_{mir} < 430\,\text{cm}^{-1}$. With a cavity length of 6.5 μm, the estimated DBR reflectivity was 75.6%, in good agreement with the simulated peak reflectivities of the three DBRs shown in Figs. 3(d)–3(f). A similar observation reveals that for the case of 2-step devices, the device with $\Lambda = 155\,\text{nm}$ obtained the lowest threshold. Here, the lasing wavelengths of the 2-step devices for $\Lambda = 150\,\text{nm}$, 155 nm, and 160 nm are $\lambda \approx 822\,\text{nm}$, 835 nm, and 848 nm, respectively. Given that $P_{th}(835\,\text{nm}) < P_{th}(822\,\text{nm}), P_{th}(848\,\text{nm})$, the only region where this threshold pump intensity condition is satisfied at a given material gain lies between points B and C—defining the upper and lower bounds, respectively. Therefore, the threshold material gain for a typical 2-step device must be in the range of 1300–2000 cm^{-1}, which is equivalent to $N_{th} = 3.8$–$5.2 \times 10^{18}\,\text{cm}^{-3}$. With the GaAs/mode overlap factor of 80%, this suggests a modal loss in the range of $650 < \alpha_{mod} < 1130$ cm^{-1}, where the calculated value is $620\,\text{cm}^{-1}$.

To assess the feasibility of electrical pumping of such a laser, the bounds on N_{th} can be linked to the lasing threshold current density, J_{th}, via $J_{th} = qN_{th}H/\tau$. Here, q is the charge of an electron, and $\tau = 1\,\text{ns}$ represents the carrier lifetime. With $N_{th} \approx 3.8$–$5.2 \times 10^{18}\,\text{cm}^{-3}$, this estimation results in a value of $J_{th} \sim$ 6–8 kA cm^{-2}.

In conclusion, we experimentally demonstrated a hybrid gap plasmon waveguide operating at room temperature, emitting in the near infrared region and exhibiting low lasing thresholds. The problem of surface recombination in GaAs was solved by growing two InGaP passivation layers on either side of the planar GaAs slab. This is possible here as our design did not require etching of the semiconductor near the laser cavity. Our gain analysis suggests that a material gain in the region of 1300–2000 cm^{-1} is required to achieve lasing—potentially achievable with a current density of approximately 6–8 kA cm^{-2}. With their simple lithographical fabrication and viability of electrical injection as a pumping mechanism, hybrid gap plasmon lasers built on suspended GaAs membranes represent a move toward practical plasmonic lasers and enable potentially greater integration into the current electronic infrastructure.

The authors would like to thank Yi Li, Themistoklis Sidiropoulos, and Sylvain Gennaro for assistance with the fabrication and characterization of the devices. This work was sponsored by the UK Engineering and Physical Sciences Research Council (EP/I004343/1 and EP/M013812/1). M.P.N. was supported by a Natural Sciences and Engineering Research Council of Canada (NSERC) scholarship and EPSRC studentship. R.F.O. was supported by an EPSRC Career Advancement Fellowship and Marie Curie IRG (PIRG08-GA-2010-277080).

[1]D. J. Bergman and M. I. Stockman, Phys. Rev. Lett. **90**(2), 027402 (2003).
[2]M. A. Noginov, G. Zhu, G. Belgrave, A. M. Bakker, R. Shlaev, V. M. Narimonov, S. Stout, E. Herz, T. Suteewong, and U. Wiesner, Nature **460**(7259), 1110–1112 (2009).
[3]R. F. Oulton, V. J. Sorger, T. Zentgraf, R. M. Ma, C. Gladden, L. Dai, G. Bartal, and X. Zhang, Nature **461**(7264), 629–632 (2009).
[4]M. T. Hill, M. Marell, E. S. Leong, B. Smalbrugge, Y. Zhu, M. Sun, P. J. Van Veldhoven, E. J. Geluk, F. Karouta, Y. S. Oei, and R. Nötzel, Opt. Express **17**(13), 11107–11112 (2009).
[5]A. M. Lakhani, M. Kim, E. K. Lau, and M. C. Wu, Opt. Express **19**(19), 18237–18245 (2011).
[6]M. J. H. Marell, B. Smalbrugge, E. J. Geluk, P. J. Van Veldhoven, B. Barcones, B. Koopmans, R. Nötzel, M. K. Smit, and M. T. Hill, Opt. Express **19**(16), 15109–15118 (2011).
[7]C. Symonds, G. Lheureux, J. P. Hugonin, J. J. Greffet, J. Laverdant, G. Brucoli, A. Lemaitre, P. Senellart, and J. Bellessa, Nano Lett. **13**(7), 3179–3184 (2013).
[8]N. Liu, A. Gocalinska, J. Justice, F. Gity, I. Povey, B. McCarthy, M. Pemble, E. Pelucchi, H. Wei, C. Silien, and H. Xu, Nano Lett. **16**(12), 7822–7828 (2016).
[9]L. Lafone, T. P. H. Sidiropoulos, and R. F. Oulton, Opt. Lett. **39**(15), 4356–4359 (2014).
[10]T. J. Duffin, M. P. Nielsen, F. Diaz, S. Palomba, S. A. Maier, and R. F. Oulton, Opt. Lett. **41**(1), 155–158 (2016).
[11]M. P. Nielsen, L. Lafone, A. Rakovich, T. P. Sidiropoulos, M. Rahmani, S. A. Maier, and R. F. Oulton, Nano Lett. **16**(2), 1410–1414 (2016).
[12]M. P. Nielsen, X. Shi, P. Ditchtl, S. A. Maier, and R. F. Oulton, Science **358**(6367), 1179–1181 (2017).
[13]M. I. Stockman, Phys. Rev. Lett. **93**(13), 137404 (2004).
[14]R. F. Oulton, G. Bartal, D. F. P. Pile, and X. Zhang, New J. Phys. **10**(10), 105018 (2008).
[15]D. Saxena, S. Mokkapati, P. Parkinson, N. Jiang, Q. Gao, H. H. Tan, and C. Jagadish, Nat. Photonics **7**(12), 963–968 (2013).
[16]B. Mayer, D. Rudolph, J. Schnell, S. Morkötter, J. Winnerl, J. Treu, K. Müller, G. Bracher, G. Abstreiter, G. Koblmüller, and J. J. Finley, Nat. Commun. **4**, 2931 (2013).
[17]M. P. Nielsen, A. Ashfar, K. Cadien, and A. Y. Elezzabi, Opt. Mater. **36**(2), 294–298 (2013).
[18]M. Wille, C. Sturm, T. Michalsky, R. Röder, C. Ronning, R. Schmidt-Grund, and M. Grundmann, Nanotechnology **27**(22), 225702 (2016).
[19]L. L. Goddard, S. R. Bank, M. A. Wistey, H. B. Yuen, Z. Rao, and J. S. Harris, Jr., J. Appl. Phys. **97**(8), 083101 (2005).
[20]Y. Li, J. Zhang, D. Huang, H. Sun, F. Fan, J. Feng, Z. Wang, and C. Z. Ning, Nat. Nanotechnol. **12**(10), 987–992 (2017).
[21]L. Lafone, T. P. Sidiropoulos, J. M. Hamm, and R. F. Oulton, IET Optoelectron. **8**(2), 122–128 (2014).
[22]W. W. Chow and S. W. Koch, *Semiconductor-Laser Fundamentals: Physics of the Gain Materials* (Springer, Berlin, 1999).
[23]B. R. Bennett, R. A. Soref, and J. A. Del Alamo, IEEE J. Quantum Electron. **26**(1), 113–122 (1990).
[24]D. D. Sell, H. C. Casey, Jr., and K. W. Wecht, J. Appl. Phys. **45**(6), 2650–2657 (1974).